Research Article Vol. 15, No. 3 / 1 Mar 2024 / Biomedical Optics Express 1976
Biomedical Optics EXPRESS

3D-printed biosensors in biomedical applications exploiting plasmonic phenomena and antibody self-assembled monolayers

FRANCESCO ARCADIO,[1] WAQAR ALI,[2] DEBORA BENCIVENGA,[2] DOMENICO DEL PRETE,[1] CHIARA MARZANO,[1] LORENA SAITTA,[3] EMANUELA STAMPONE,[2] ROSARIO CENNAMO,[2] VINCENZO CARAFA,[2,4] LUCIA ALTUCCI,[2,4,5,6] LUIGI ZENI,[1] GIANLUCA CICALA,[3] AND NUNZIO CENNAMO[1,*]

[1]*Department of Engineering, University of Campania Luigi Vanvitelli, 81031 Aversa, Italy*
[2]*Department of Precision Medicine, University of Campania Luigi Vanvitelli, 80138 Naples, Italy*
[3]*Department of Civil Engineering and Architecture, University of Catania, Viale Andrea Doria 6, 95125 Catania, Italy*
[4]*Biogem Institute of Molecular and Genetic Biology, 83031 Ariano Irpino, Italy*
[5]*Institute of Endocrinology and Oncology "Gaetano Salvatore" (IEOS), 80131 Naples, Italy*
[6]*Program of Medical Epigenetics, Vanvitelli, Hospital, 80138 Naples, Italy*
[*]*nunzio.cennamo@unicampania.it*

Abstract: In this work, a 3D-printed plasmonic chip based on a silver-gold bilayer was developed in order to enhance the optical response of the surface plasmon resonance (SPR) probe. More specifically, numerical and experimental results were obtained on the 3D-printed SPR platform based on a silver-gold bilayer. Then, the optimized probe's gold plasmonic interface was functionalized with a specific antibody directed against the $p27^{Kip1}$ protein (p27), an important cell cycle regulator. The 3D-printed plasmonic biosensor was tested for p27 detection with good selectivity and a detection limit of 55 pM. The biosensor system demonstrated performance similar to commercially available ELISA (enzyme-linked immunoassay) kits, with several advantages, such as a wide detection range and a modular and simple-based architecture. The proposed biosensing technology offers flexible deployment options that are useful in disposable, low-cost, small-size, and simple-to-use biochips, envisaging future applications in experimental and biomedical research.

1. Introduction

Nowadays, the need for low-cost, disposable, and easily transportable sensors to be used in several application areas has achieved increasing importance. In this regard, 3D printing technology has recently emerged as a great alternative to the realization of electronic and optoelectronic devices, which are typically produced using expensive materials, instrumentation, and technological processes [1]. In this regard, systems made entirely of plastic offer several benefits over silicon-based ones, such as from an economical point of view, since the use of fast-prototyping equipment, like 3D printers, is extremely advantageous and less cumbersome than the one used to realize silicon-based systems [1,2]. This kind of sensor system also represents a great achievement for biosensor applications in terms of cost, versatility, and capability to detect several substances with high sensitivity and excellent resolution [3–5]. In this application field, great relevance was attained by disposable devices so that when the chip comes into contact with toxic substances or dangerous viruses, after a diagnostic test, it can be immediately read and thrown away, reducing the risk of contamination for the test operator. In this regard, the setup used to perform this type of test is extremely simple, so it does not demand the help of a specialized operator [6–9].

#516565 https://doi.org/10.1364/BOE.516565
Journal © 2024 Received 20 Dec 2023; revised 19 Jan 2024; accepted 19 Jan 2024; published 29 Feb 2024

Biomedical Optics EXPRESS

In the last few years, sensors based on Surface Plasmon Resonance (SPR) have been used in several applications, such as for the detection of chemical and biological species, healthcare, industrial applications, and liquid concentration measurements [10–13]. The SPR is a very sensitive technique able to detect the refractive index changes at the interface between a dielectric medium and a metallic nanolayer; the latter can be either a single layer (e.g., gold, silver etc. [14,15]) or a combination of several metals [16,17]. In particular, when the resonance condition is satisfied, a dip appears in the transmission spectra at a specific wavelength, called resonance wavelength, which depends on the refractive index at the interface between the dielectric medium and the metallic layer [18–22].

Hinman et al. recently pointed out the successful combination of 3D printing technologies and SPR techniques with the development of a plasmonic biosensor based on 3D-printed equilateral prisms and photoactive resins [23]. Along this line, Cennamo et al. [24] presented an innovative 3D-printed SPR platform based on photocurable resins covered by a gold nanofilm. The same authors recently proposed preliminary results about the same 3D-printed platform covered by a metal bilayer (silver and gold) to enhance plasmonic performance [25].

Generally, low-cost and highly sensitive optical biosensors are needed for pre-analytical studies in biomedical applications, such as determining the appropriate dosage of extracellular or intracellular analytes. In this case, the selection of a specific diagnostic test might be addressed by plasmonic biosensors, which could offer prompt and useful information [9–11].

In this work, an improved version of the platform presented in [25] is proposed by optimizing the metal film bilayer (silver and gold) thicknesses by means of numerical simulations. The optimized plasmonic sensor configuration is then experimentally tested as a refractometer. Moreover, after a functionalization process, the optimized plasmonic platform was used to carry out p27 detection in the buffer solution. Also, a selectivity test was carried out to highlight the high specificity of the proposed sensing approach. Lastly, for the sake of comparison, the same functionalization process was repeated for a conventional SPR platform based on plastic optical fibers (POFs) [14], validating the 3D-printed biosensing technology proposed here.

The p27 is an important cell proliferation gatekeeper, whose levels and cellular localization, and mainly mutations of its encoding gene, have been associated with cancer onset and progression. The importance of this protein lies in its crucial role in cellular physiology. Particularly, cell proliferation control is the most studied function performed by the protein via its flexible structure [26], owing to its ability to selectively bind and inhibit Cyclin/Cyclin-dependent kinase complexes [27]. Importantly, p27 levels, localization, and post-translational modifications have been correlated to cancer treatment efficacy or chemotherapy sensitivity [28–30].

To our knowledge, this is the first example of a portable biosensor for p27 detection presented in the literature. In fact, only commercial kits, such as those used for Enzyme-linked immunosorbent assays with similar LODs or other highly complex and expensive analytical approaches, are currently available for this measurement.

2. Materials and methods

2.1. Sensor's materials

The materials used for the biosensor manufacturing are two different grades of clear resin: VeroClear RGD810 and Norland Optical Adhesive NOA88. The first one was used on a 3D printer Stratasys Objet260 Connex 1 (Stratasys, Los Angeles, CA, USA) to manufacture the structure of the device. It is an acrylic liquid photopolymer characterized by the following specifications: (i.) refractive index equal to 1.531 at 650 nm; (ii.) tensile modulus of 2.5 GPa; (iii.) heat distortion temperature (HDT) ranging between 45 and 50°C; (iv.) it is stiff at room temperature. Furthermore, its chemical formulation is proprietary since it was industrialized by Stratasys for the PolyJet 3D printing technique. However, according to its safety data sheet (SDS), the chemical formulation is a complex compound of acrylate monomers and photoactivators.

Biomedical Optics EXPRESS

Regarding the 3D printing process, the FullCure705 was used as a breakaway sacrificial material (support), used near complex geometries (overhangs and holes), and easily removable by water jetting. According to its SDS, it is a complex mixture of acrylic liquid photopolymer, polyethylene glycol, propane-1,2-diol, and glycerol. Both VeroClear RGD810 and FullCure705 were purchased from OVERMACH S.p.A. (Parma, Italy).

Next, the waveguide core of the 3D-printed biosensor was realized by using an UV photocurable resin, whose trade name is NOA88, and which was purchased from Edmund Optics LTD (UK). The latter presents the properties listed below: (i.) refractive index of 1.56 at 589 nm; (ii.) low viscosity, equal to 250cps; (iii.) UV-curable within the range 315-395 nm. In agreement with the last property, it was cured by exploiting a universal lamp bulb with UVA emission at 365 nm.

2.2. 3D-printed sensor platform design and manufacturing process

Starting from a similar design developed by the authors to realize a 3D-printed microstructured surface plasmon resonance (SPR) sensor [24,25], an enhanced version was designed and realized in order to develop a plasmonic biosensor. Even in this case, the 3D printed platform was designed as an assembly of four distinctive parts: (i.) a substrate, acting as the cladding of the waveguide; (ii.) the input and output plastic optical fibers (POFs) supports; (iii.) a cover to properly store the 3D-printed platform; (iv.) a customized mask for the metal sputtering on the waveguide's core. Additionally, the mating system was improved in the new proposed design. The latter will also be useful to realize sensor's lapping post-treatment in correspondence with the input and output waveguide region.

Figure 1 reports both the CAD design and the 3D printing of the components, i.e., substrate, input/output POFs' supports, cover for storage, and customized mask for sputtering.

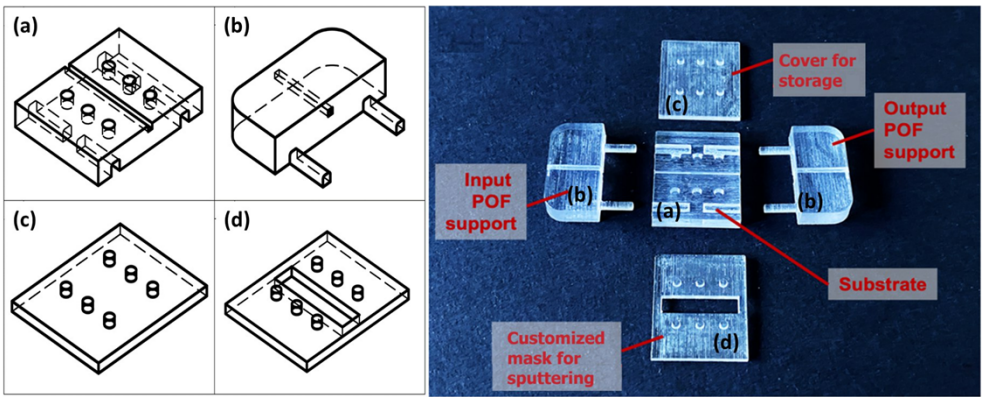

Fig. 1. CAD design and 3D printing of: (a) substrate; (b) plastic optical fibers' supports; (c) cover for storage; (d) customized mask for sputtering.

In particular, the substrate was modelled as having a linear channel with a square section of 1.2×1.2 mm^2. The latter size was adequately selected in the modelling phase by taking into account the accuracy of the chosen 3D printing technique for the sensor manufacturing. Indeed, since the channel's width must have a nominal size of 1 mm, an offset of 200 µm (bias setup) with respect to the nominal size was set. Moving on to the input/output POFs' supports, they were modelled correctly to ensure a proper alignment between the POFs itself and the platform's waveguide core. In fact, they present a square-section hole that fits the POFs size. More specifically, the two supports for the launch and collection POFs include a trench that was custom-designed and 3D-printed to accommodate the fibers and to interlock them with the 3D-printed sensor, as reported in Fig. 2(a). Thanks to these supports, the launch and collection

Biomedical Optics EXPRESS

POFs go into contact with the core of the waveguide. Moreover, to guarantee a solid coupling between the latter and the substrate, a slipping mating system was designed: the groovings are predisposed in the substrate, while the gliding elements are inserted in the POFs supports (see Fig. 2(a)).

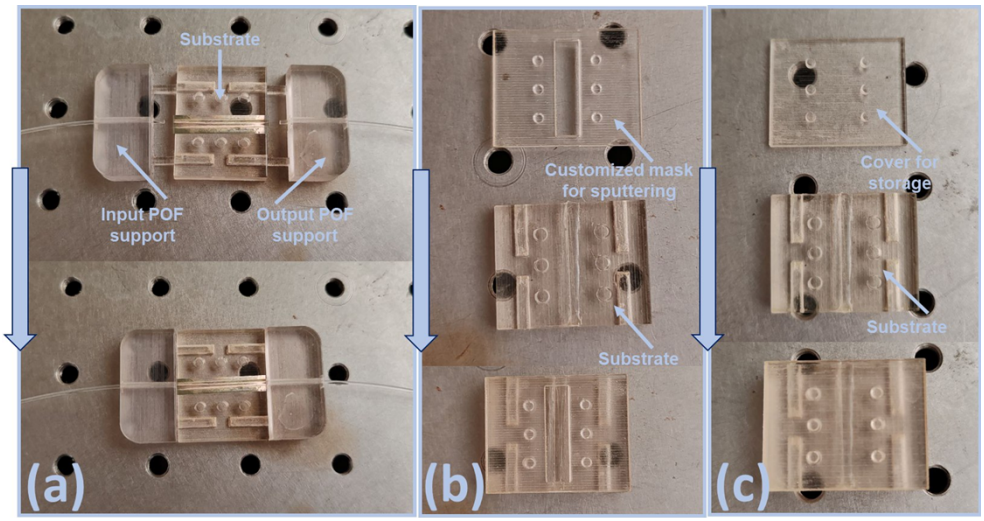

Fig. 2. Actual images of 3D-printed components and their assemblies for a) usage, b) sputtering process and c) storage.

Regarding the customized mask, it was modelled to perform a uniform deposition on the waveguide core with an Ag-Au bilayer by using the sputtering method, as depicted in Fig. 2(b). Finally, the cover, useful for the probe storage, was modelled starting from the substrate's geometry, to ensure a perfect fitting through a hole-pin system (see Fig. 2(c)).

The latter metal deposition was necessary to trigger the SPR phenomenon. Thus, starting from the waveguide core's size, the window's area of the mask was adequately sized to avoid shadow areas during the sputtering deposition: it has a width of 3 mm, which is 1.8 mm larger than the waveguide core.

The manufacturing of each part described so far was accomplished by following a generic additive manufacturing process flow that consists of the following steps:

1. Conceptualization development and Computer-Aided Design development – this step was carried out by exploiting Autodesk Fusion 360 as modelling software;
2. STL generation – once the CAD for each part of the biosensor was ready, the STL format was exported;
3. STL transfer on 3D printing machine – the STL file was handled with the proprietary software Objet StudioTM, with the aim to create the G-Code commands for the used 3D printing machine;
4. Manufacturing process – the biosensor was fabricated by using a PolyJet 3D printer Stratasys Objet260 Connex 1, so by jetting tiny droplets for the selected photocurable resin (VeroClear RGD810) on a build platform and by photo-curing the same using a UV light. The jetting of the photopolymer was performed in detail through an inkjet print head, while the UV light source was placed in the print head itself.

Biomedical Optics EXPRESS

Figure 3 reports a schematization of the designed plasmonic platform, with the substrate (cladding) and waveguide core dimensions, while the step-by-step manufacturing process to realize it is reported in Fig. 4.

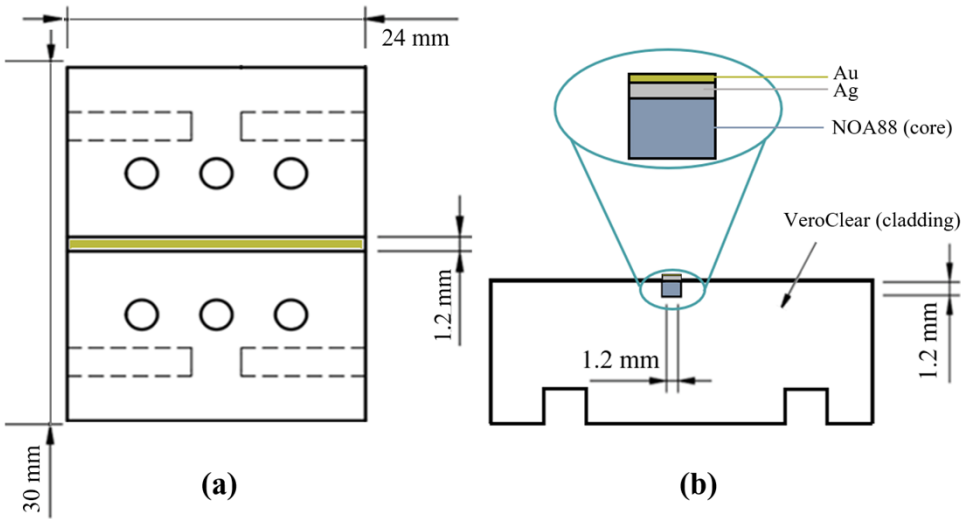

Fig. 3. Outline of the designed and realized plasmonic platform: a) top view and b) cross-section.

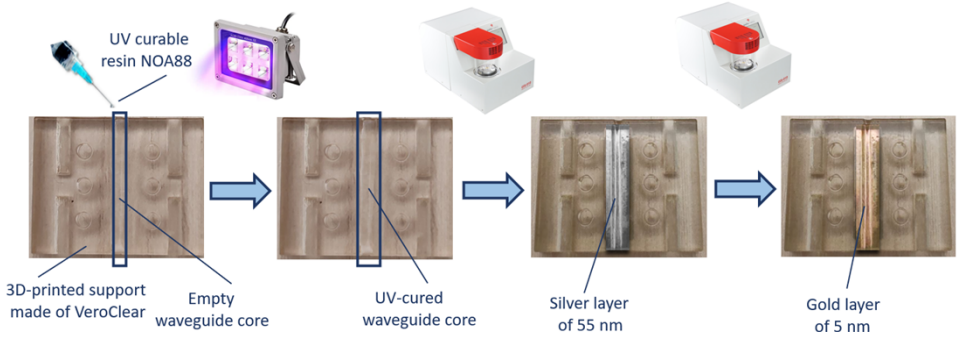

Fig. 4. Step-by-step 3D-printed plasmonic probe manufacturing process.

More specifically, once the components were 3D-printed, the channel predisposed in the substrate was filled with the NOA88 optical adhesive for the waveguide core fabrication. In fact, it was microinjected into the channel using a syringe equipped with a 0.5 mm gauge. Next, it was UV-cured for 10 minutes using a universal lamp bulb with an emission at 365 nm.

It is important to underline that the optical adhesive (core, made of NOA88 optical adhesive) was injected in such a way as to fill the channel present inside the substrate (cladding, made of VeroClear), as reported in Fig. 4, so avoiding gap between core and cladding. Moreover, in the biosensing application reported, we used a polymer-based waveguide (exploiting NOA88/VeroClear) reported in [24,25] and optimized the thicknesses of the metal bilayer to improve the plasmonic performance. Additional fabrication steps like polishing procedures to planarize the waveguide's core surface or a metal deposition, acting as a mirror for light propagation, between the cladding and the core, could be introduced to further enhance the performance.

Biomedical Optics EXPRESS

In the end, to trigger the SPR phenomenon, the metal bilayer (Ag-Au) was deposited using the customized 3D-printed mask (as for Fig. 2(b).). In detail, an Ag layer thick 55 nm was deposited on the waveguide core via sputtering deposition using a sputter coater machine (Safematic CCU-010, Zizers, Switzerland). The Ag deposition process was performed under the following conditions: time of deposition of 62 s, pressure of 0.05 mbar and current of 60 mA. Next, upon the Ag film, an additional Au film was deposited with a thickness of 5 nm. Even the latter was deposited through a sputtering deposition method, which was carried out for 5 s at 0.05 mbar of pressure and with a current of 60 mA.

2.3. SPR-POF reference sensor

The construction process of the SPR-POF reference sensor is described in [14]. It includes a POF with a PMMA core of 980 µm diameter and a cladding of 10 µm diameter (1 mm total diameter). The POF was fixed in a resin block and then lapped using two different polishing papers (1 µm and 5 µm grits) to obtain a D-shaped section. After this, a 1 µm thick photoresist buffer layer (Microposit S1813) is deposited on the exposed core by using a spin coater. The photoresist buffer layer is used to improve both the optical performances (in terms of refractive index range of detection) and the metal adhesion on the D-shaped POF. In the end, a 60 nm thick gold film is deposited by using a sputtering machine (Safematic CCU-010, Zizers, Switzerland). Figure S1. in the Supplemental document (Supplement 1) shows a schematic cross-section of the SPR-POF platform.

2.4. Chemicals and reagents for the receptor layers

N-(3-Dimethylaminopropyl)-N′-ethylcarbodiimide hydrochloride (EDC), N-Hydroxysuccinimide (NHS), Ethanolamine, (±)-α-Lipoic acid, phosphate buffered saline (PBS), Tween 20 were purchased from Merck KGaA (Darmstadt, Germany). The mouse monoclonal antibody against p27 was from BD Transduction Laboratory. Human recombinant p27 protein was furnished by OriGene Technologies, Inc. (Rockville, MD, USA). All the reagents were at the maximum degree of purity, and all the used solutions, prepared just before the use, were obtained by using ultrapure Milli-Q water (Milli-Q IQ 7000, Merk) and were filtered with 0.2 µm pore diameter filters before the use.

2.5. Binding experiments in phosphate buffer saline

The binding measurements of the developed SPR biosensor were obtained by dropping human recombinant p27 (hrp27) at different concentration values over the sensing area. Firstly, a solution of hrp27 was dissolved in PBS at 1 µM concentration. Then, serial dilutions were obtained by using filtered PBS, and 0.1, 0.25, 0.5, 1, 2, 5, 10, 20, and 50 nM solutions were prepared.

To obtain the dose-response curve, about 50 µL each dilution was dropped over the sensing region of both the SPR-POF and 3D-printed biosensors and incubated at room temperature for five minutes, sufficient for the interaction with the immobilized antibody. After a washing step with PBS, the spectrum was acquired with PBS as a bulk solution at the end of each incubation step.

Regarding the selectivity tests, different solutions were prepared using hrp27, MMP-2, and IL-6, separately, all at the same concentration value of 1 nM. By adopting the previously described measure protocol, 50 µL of each solution was analyzed by the sensors functionalized with anti-p27 antibody.

3. Receptor self-assembled monolayer: functionalization process

The immobilization process was performed as reported in [31]. Precisely, the POF and 3D-printed surfaces were sequentially cleaned with Milli-Q water (3 times, 5 minutes each time)

Biomedical Optics EXPRESS

and 8% ethanol in Milli-Q water (3 times for 5 min). Then, the metal nanofilm covering both biosensing platforms POF (60 nm of Au thickness) and 3D-printed (Ag/Au = 55/5 nm) was treated for 18 h at room temperature with lipoic acid at a final concentration of 0.3 mM in 8% ethanol solution: the lipoate addiction was useful to produce a surface exposing carboxyl groups, destined for the next activation, that was performed with N-Hydroxysuccinimide/N-(3-Dimethylaminopropyl)-N′-ethylcarbodiimide hydrochloride mixture (NHS/EDC, 200 mM/50 mM in PBS pH7.4, respectively). The last step of activation was carried out for 20 minutes at room temperature, and three washes with PBS were performed to eliminate the excess of the used reagents; afterwards, the surfaces were incubated for 2 h at room temperature with 20 µL anti-p27Kip1 antibody (0.25 mg/mL) for covalent immobilization on both biosensors. After three washes with PBS for antibody excess removal, the free remaining activated carboxyl groups were blocked by incubating the functionalized surfaces with 1 M ethanolamine, pH 8.0, for 30 min at room temperature. For this step, 0.005% Tween20 was added to PBS, and then, the functionalized platforms were stored in PBS overnight at 4°C before use. The various steps of the functionalization procedure are outlined in Fig. 5.

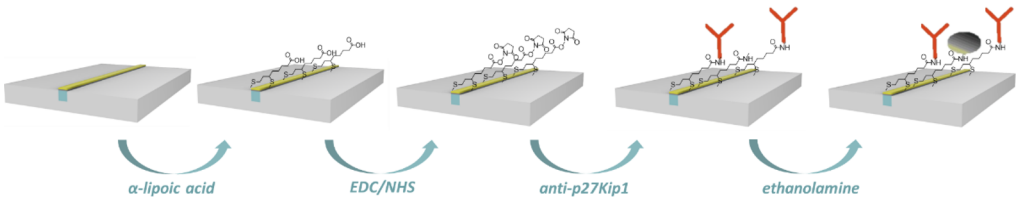

Fig. 5. Outline of the step-by-step functionalization procedure.

4. Numerical analysis and experimental setup

4.1. Theoretical background and numerical analysis

In order to characterize the optical sensor system, it is necessary to define the sensitivity, resolution, and figure of merit (FOM). In particular, the sensitivity can be defined as follows [14]:

$$S(n) = \frac{\delta\lambda}{\delta \mathrm{n}} \left[\frac{nm}{RIU}\right] \tag{1}$$

where δλ is the variation in resonance wavelength caused by a variation in the external refractive index of δn. Another parameter of interest is the resolution (**Δn**) defined as the minimum variation in refractive index that can be detected, which can be defined as [14]:

$$\Delta n = \frac{\delta \mathrm{n}}{\delta\lambda}\,\delta\lambda_{DR} = \frac{1}{S(n)}\,\delta\lambda_{DR}\,[RIU] \tag{2}$$

where $\boldsymbol{\delta\lambda_{DR}}$ is the resolution of the spectrometer used for the experimental tests.

Lastly, the FOM is a well-known quantitative indicator to describe the SPR sensor performance, and it can be defined as follows as the ratio between sensitivity and the full width at half maximum (FWHM) of the SPR curve [32,33]:

$$FOM(n) = \left.\frac{S}{FWHM}\right|_n \tag{3}$$

A numerical analysis was performed by using an N-layer approximation and exploiting the transfer matrix formalism in a similar way to [25], as described in [34–36]. In [25], a 3D-printed waveguide was designed and simulated by considering the thickness of 30 nm of silver (Ag) and

Biomedical Optics EXPRESS

30 nm of gold (Au). Starting from this work [25] and by using the numerical model previously described, different bilayer configurations were simulated by varying the thickness of the two metal layers, i.e., silver (Ag) and gold (Au). In such a way, it was possible to compare several bilayer-based sensor configurations in terms of sensitivity. For completeness, the numerical results achieved by tuning the thicknesses of the silver-gold bilayer are reported in Fig. S2. of the Supplemental document (Supplement 1).

Figure 6(a) shows the results obtained by simulating the configuration with 55 nm of Ag and 5 nm of Au, along with a quadratic fitting of the simulated values, while Fig. 6(b) shows the sensitivity obtained as the first derivative (as for Eq. (1)) of the quadratic fitting function reported in Fig. 6(a). It is clear from Fig. 6(b) that the numeric sensitivity depends on the refractive index of the solution in a linear way.

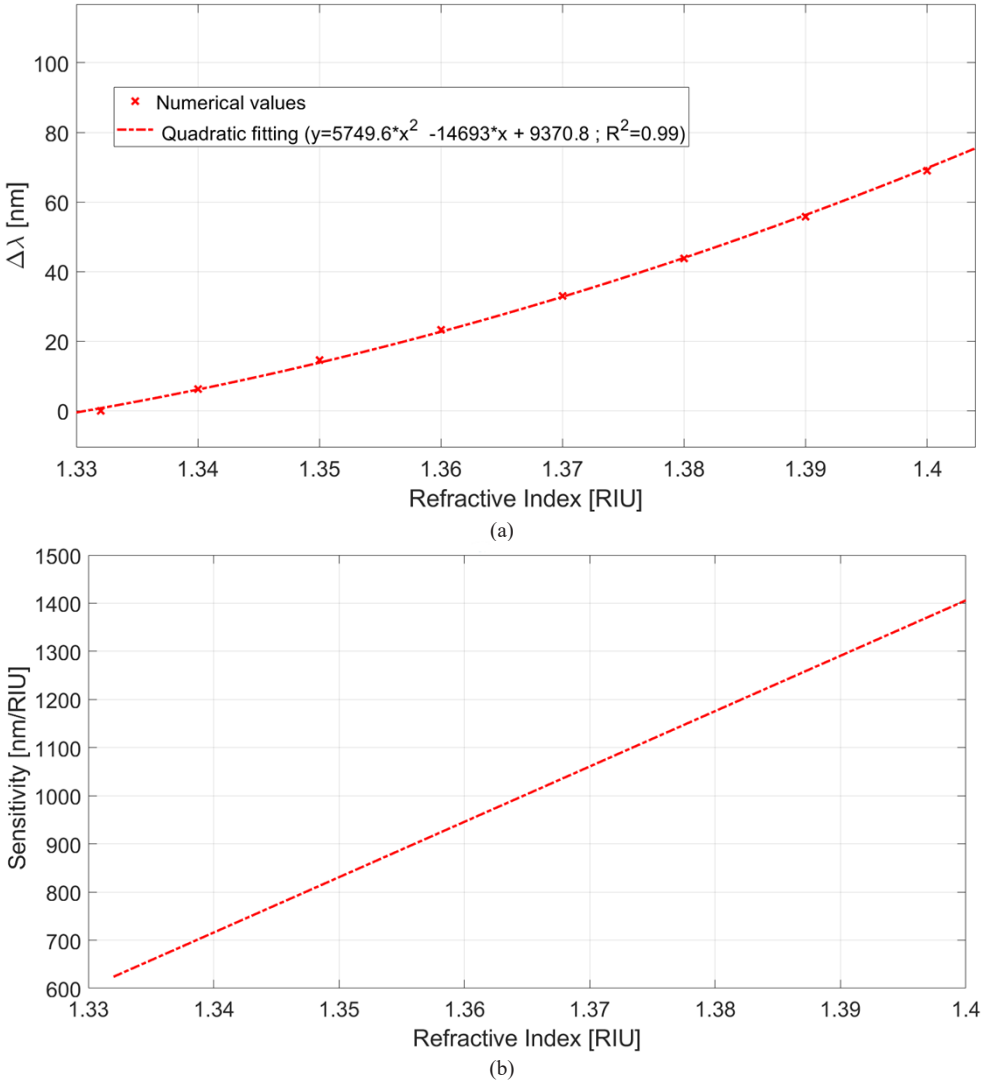

Fig. 6. Simulated bilayer configuration based on 55 nm of Ag and 5 nm of Au: (a) numerical values (red cross) and quadratic fitting (dashed line) of the simulated values; (b) sensitivity as a function of the external refractive index.

Biomedical Optics EXPRESS

From the numerical results, the configuration with 55 nm thickness of Ag and 5 nm thickness of Au improved with respect to the other simulated configurations and the experimental configuration previously presented in [25]. In fact, comparing the presented configuration with that proposed in [25], about 25% improvement in simulated bulk sensitivity is achieved.

It should also be stressed that, as it is well-known from the literature, in the case of SPR sensors based on optical waveguides and metallic multilayer, the plasmonic performances are highly influenced by both the disposition order of the metals and their thicknesses as well as by the optical properties of the utilized waveguide (core and cladding) [17,35,37–39]. Standing this, in the present work, by fixing the waveguide optical properties and by choosing the metals composing the bilayer (silver and gold), we optimized the thicknesses of the two metallic layers by taking advantage of transfer matrix formalism assuming an N-layer model [17,34,40–42].

4.2. Experimental setup

A simple and low-cost experimental setup was used to test the described platform. In particular, it consists of a white light source and a spectrophotometer. The 3D-printed platform was placed between the white light source (HL–2000–LL, manufactured by Ocean Optics, Dunedin, FL, USA), having an emission range from 360 nm to 1700nm, and the spectrometer (FLAME-S-VIS-NIR-ES, Ocean Optics, Orlando, FL, USA) having a detection range between 350 nm and 1000 nm.

Two POF patches (Ø1 mm) were used to guide the input and output light. Finally, the spectrophotometer is connected to the laptop in order to acquire and process the data. Figure 7 shows an actual image of the experimental setup used to test the SPR 3D-printed bilayer sensor. The same experimental equipment was also used to test the SPR-POF reference sensor.

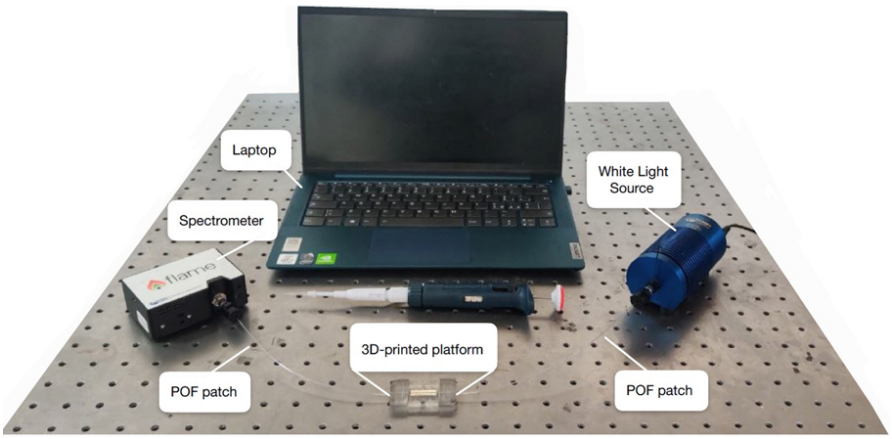

Fig. 7. Picture of the experimental setup.

The spectrometer is connected to a laptop to process the data using Matlab software. More specifically, all the experimental values (SPR spectra) were smoothed through the "smooth" Matlab function (smooth factor equal to 120). Next, through a customized script, the smoothed SPR spectrum is further windowed in proximity to the dip and smoothed a second time to reduce the noise near the minimum of the function (smooth factor equal to 10). Downstream from the smoothing processes, it is possible to use a standard Matlab function to determine the minimum of the windowed function, hence the resonance wavelength.

Biomedical Optics EXPRESS

5. Experimental results and discussion

5.1. Optical response

First, the 3D-printed platform was optically tested as a refractometer by means of solutions with different refractive indices. In particular, the analyzed solutions were obtained by mixing water and glycerine in different percentages to obtain refractive indices values between 1.332 and 1.382 RIU. Before use, these values were confirmed by a commercial Abbe refractometer (model RMI, Exacta Optech, Germany).

The acquired transmitted spectra at different solutions are normalized on the reference spectrum (the transmitted spectrum acquired without solutions, in air, where the SPR condition is not satisfied) to achieve the SPR spectra. Figure 8 shows the SPR spectra obtained by different external refractive indices (different solutions). As shown in Fig. 8, when the refractive index of the solution changes, the resonance wavelength shifts to higher values (red-shift).

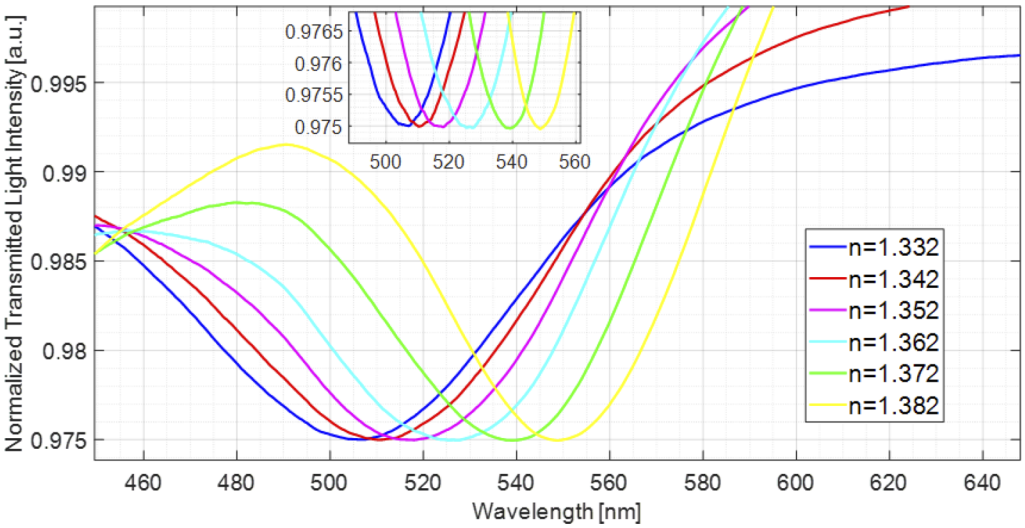

Fig. 8. Experimental SPR spectra for different values of external refractive indices.

In order to make a comparative analysis between the optimal configuration (Ag 55 nm - Au 5 nm) and that previously presented in [25] (Ag 30 nm - Au 30 nm), in Fig. 9(a) the experimental values fitted by quadratic functions for both configurations are shown. In particular, the Equation used to fit the experimental values can be defined as follows:

$$\Delta\lambda = An^2 + Bn + C \tag{4}$$

Table 1 reports the values of the A, B, and C coefficients for both the compared configurations based on the same 3D-printed waveguide and on different metal bilayers. For completeness, Fig. S3. of the Supplemental document (Supplement 1) compares numerical and experimental results attained by the optimized configuration (Ag 55 nm - Au 5 nm).

Table 1. Coefficients of the quadratic fitting curves for both configurations: 30 nm Ag-30 nm Au and 55 nm Ag-5 nm Au.

Configuration	A	B	C	R^2
30 nm Ag - 30 nm of Au [25]	3553.6	8834.7	5462.7	0.99
55 Ag - 5 nm of Au	9500	24901	16313	0.99

Biomedical Optics EXPRESS

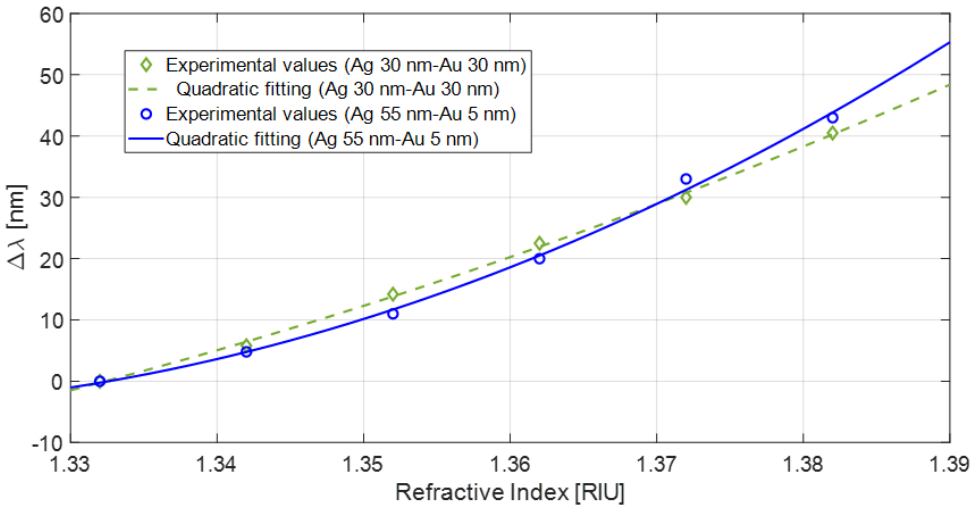

(a)

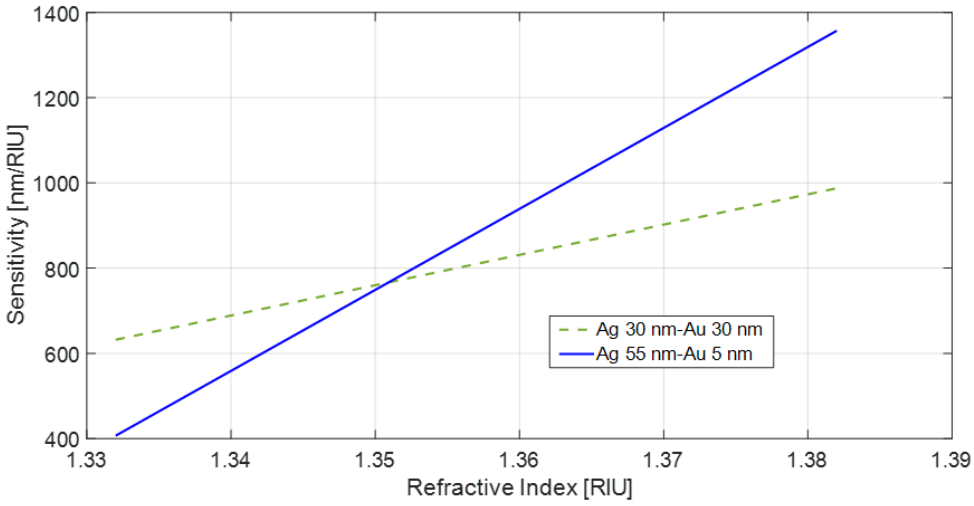

(b)

Fig. 9. (a) Experimental values (marker) and quadratic fitting (solid and dotted lines) and (b) sensitivity calculated for both configurations, i.e., 30 nm Ag-30 nm Au [25] and 55 nm Ag-5 nm Au.

Figure 9(b) shows the experimental sensitivities obtained using the quadratic fitting functions reported in Fig. 9(a) and Eq. (1). It can be seen from Fig. 9(b) that the configuration proposed in this work (Ag 55 nm-Au 5 nm) shows a clear improvement in sensitivity for refractive indices greater than 1.35 RIU.

In general, SPR sensors based on multimodal waveguides (like the one presented in this work) are characterized by a greater sensitivity but higher FWHM values with respect to SPR configurations based on monomodal waveguides [34,43]; thus, the FOM values related to monomodal-based configurations are typically greater than the ones of multimodal-based configurations. In the presented case, the FOM was calculated at n = 1.38 and resulted equal

Biomedical Optics EXPRESS

to about 21 RIU^{-1}. This FOM value is similar to other SPR sensors based on monomodal waveguides (FOM values between 15 and 20) [44].

5.2. Binding tests

As a proof of concept, the optimized SPR platform presented in this work was functionalized for p27 detection (as described in Section 3) to carry out the binding tests. Figure 10 shows the normalized transmitted spectra, acquired before and after the functionalization process, with water as an encompassing medium (the bulk solution) to analyze the functionalization procedure's effectiveness.

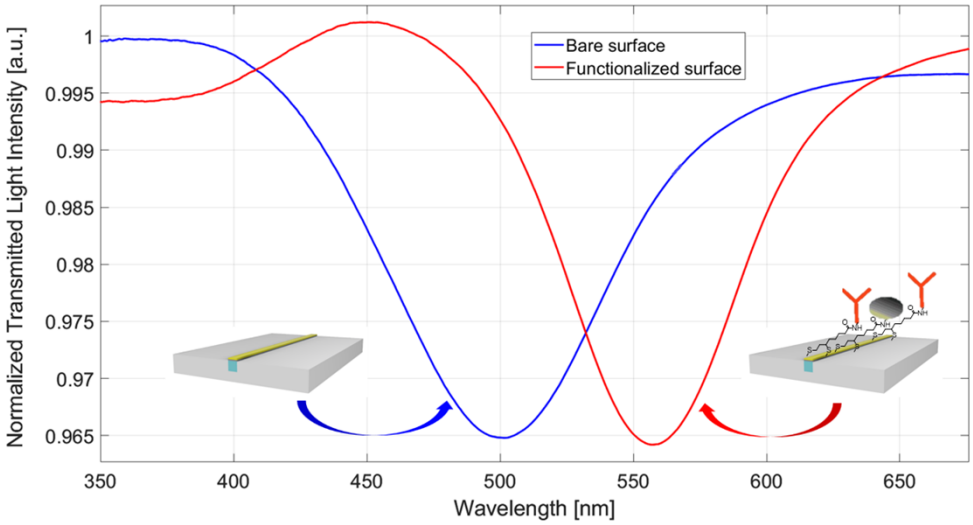

Fig. 10. Normalized transmitted spectra acquired with water before (blue line) and after (red line) the functionalization process.

Figure 10 shows that the resonance wavelength, after the functionalization process, shifts to about 56 nm, thus confirming the correct receptor immobilization onto the sensitive surface. Furthermore, the obtained variation in resonance wavelength corresponds to a working point of about 1.38 RIU (as for Fig. 9(a)), where the configuration Ag 55 nm - Au 5 nm overperforms the Ag 30 nm - Au 30 nm one in terms of sensitivity (see Fig. 9(b)).

After this, the 3D-printed plasmonic biosensor was tested using the solution with different concentrations of the analyte (p27) between 0.1 nM and 50 nM. Figure 11(a) shows the SPR spectra obtained at the indicated p27 concentration values. As it is clear, a resonance wavelength shift towards the left (blue-shift) at increasing analyte concentrations was achieved. This trend is similar to that obtained in previous works [31,45] and involves a change in the receptor's conformation following the binding. The bio-receptor refractive index decreases when the binding with the analyte occurs.

Figure 11(b) shows the absolute resonance wavelength variation (calculated with respect to the resonance wavelength of the blank) as a function of the analyte concentration with the Langmuir fitting of the experimental data, defined in the following Hill Equation with n = 1:

$$|\Delta\lambda_c| = |\lambda_c - \lambda_0| = |\Delta\lambda_{max}| \cdot \left(\frac{c^n}{K^n + c^n}\right) \tag{5}$$

Where c represents the concentration of the analyte, λ_c is the resonance wavelength at concentration c, λ_0 is the resonance wavelength of the blank, $\Delta\lambda_{max}$ is the difference between the resonance

Biomedical Optics EXPRESS

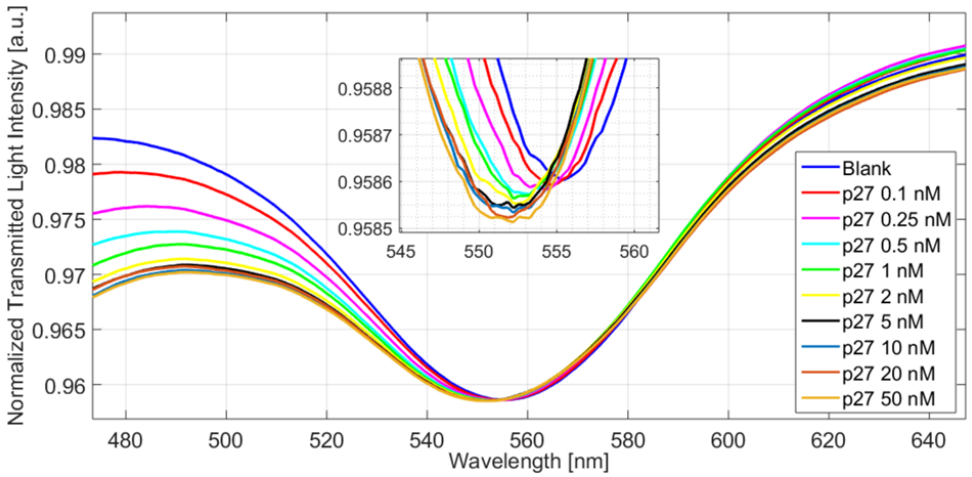

(a)

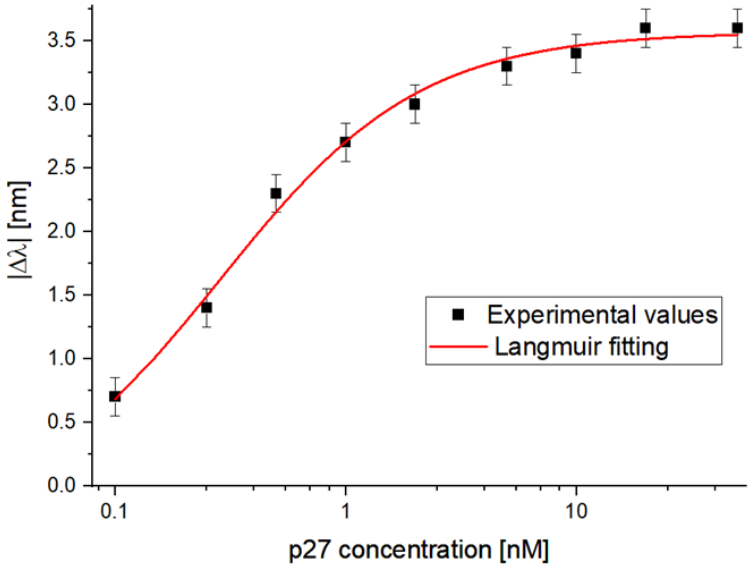

(b)

Fig. 11. (a) SPR spectra obtained by the 3D-printed biosensor for different values of p27 concentration. (b) Absolute value of the experimental variation in resonance wavelength (black marker), calculated with respect to the resonance wavelength of the blank, with relative error bars. The Langmuir fitting (red line) of the experimental values is also reported.

wavelength at saturation value and the blank. Generally, the parameters n and K are the Hill fitting constants. When n equals 1, the Hill model coincides with the Langmuir model (as in this case) and $K = 1/K_{aff}$, where K_{aff} represents the affinity constant.

The error bars reported in Fig. 11(b) were calculated as the maximum standard deviation of the dataset ($n = 3$), the latter indicating the number of measurements performed on different biosensors in similar working conditions.

From the Langmuir fitting parameters (reported in Table 2), it is possible to calculate the characteristic performance parameters of the biosensor, i.e., the sensitivity at low concentration,

Biomedical Optics EXPRESS

the affinity constant, and the limit of detection (LOD) [46]. More specifically, for low values of the analyte concentration, in other words, for values of c much lower than K, Eq. (5) can be considered linear and the sensitivity at low concentrations of the sensor is defined as the slope ($|\Delta\lambda_{max}|/K$) of the linear function. In this case, it assumes the value of about 13.77 nm/nM. This parameter is useful for calculating the LOD, which can be estimated as the ratio of three times the standard deviation of the blank (St. error of λ_0 in Table 2) and the sensitivity at low concentration. Therefore, the LOD value is equal to about 55 pM.

Table 2. Langmuir fitting parameters of the two analyzed configurations.

Sensor	λ_0 [nm]		$\Delta\lambda_{max}$ [nm]		K [nM]		Statics	
	Value	St. error	Value	St. error	Value	St. error	Value	St. error
3D-printed biosensor	-0.33	0.25	3.57	0.05	0.28	0.05	0.40	0.99
SPR-POF biosensor	-1.01	0.81	2.08	0.09	0.11	0.06	0.46	0.97

Finally, the affinity constant, defined as the reciprocal of the K parameter (Table 2), is equal to about 3.53 nM^{-1}.

In order to verify the selectivity of the 3D-printed plasmonic biosensor, the functionalized platform was tested with two interferents, Matrix Metalloproteinase-2 (MMP-2) and Interleukin-6 (IL-6), and the substance of interest (p27), all diluted at the final concentration of 1 nM.

Figure 12(a) reports the SPR spectra for the three analyzed solutions at the same concentration (1 nM). As it is clear from the SPR spectra of Fig. 12(a) and the $\Delta\lambda$ shifts reported in Fig. 12(b), both MMP2 and IL-6 produce a slight resonance wavelength variation (less than 0.3 nm), whereas the p27 produces a significant resonance wavelength variation (about 2 nm), hence confirming the high selectivity of the proposed 3D-printed biosensor.

Finally, the same binding test was performed on a conventional SPR-POF platform [14], functionalized similarly, to compare the obtained biosensing performance with those achieved by exploiting the proposed 3D-printed biosensor. Figure S4 of the Supplemental document (Supplement 1) shows the SPR spectra achieved by the binding tests via an SPR-POF probe. The reference SPR-POF biosensor was tested with the same analyte concentrations used for the 3D-printed biosensor. Figure 13 shows the relative dose-response curve with the Langmuir fitting of the experimental values and the error bars. In the same way as for the tested 3D-printed biosensor, the sensitivity at low concentrations, the affinity constant, and the LOD were also calculated for the reference SPR-POF biosensor using the parameters reported in Table 2.

The Langmuir fitting parameters of both sensor configurations are shown below in Table 2.

Table 3 reports the binding parameters for both the analyzed SPR biosensor configurations. As it is clear from Table 3, the two biosensor configurations denoted very similar performances.

Table 3. Comparative analysis between 3D-printed and SPR-POF biosensors.

Sensor	LOD [pM]	K_{aff} [nM^{-1}]	Sensitivity at low c [nm/nM]
3D-printed platform	55	3.53	13.77
SPR-POF platform	91	8.66	26.78

Furthermore, from Fig. 13, it can be seen that the saturation of the sites was reached at the concentration of 2 nM. Figure 11(b) shows that the plateau of the proposed p27 biosensor was reached at the concentration of 20 nM. This substantial difference is caused by the fact that the sensing region of the 3D-printed biosensor is longer dimensionally than the sensing region of the SPR-POF biosensor. As a result, the number of specific sites on the 3D-printed platform is greater than the one on the SPR POF platform and consequently, the saturation is reached for higher analyte concentrations in the case of the 3D-printed platform. This aspect is also confirmed by the resonance wavelength variation obtained before and after the functionalization

Biomedical Optics EXPRESS

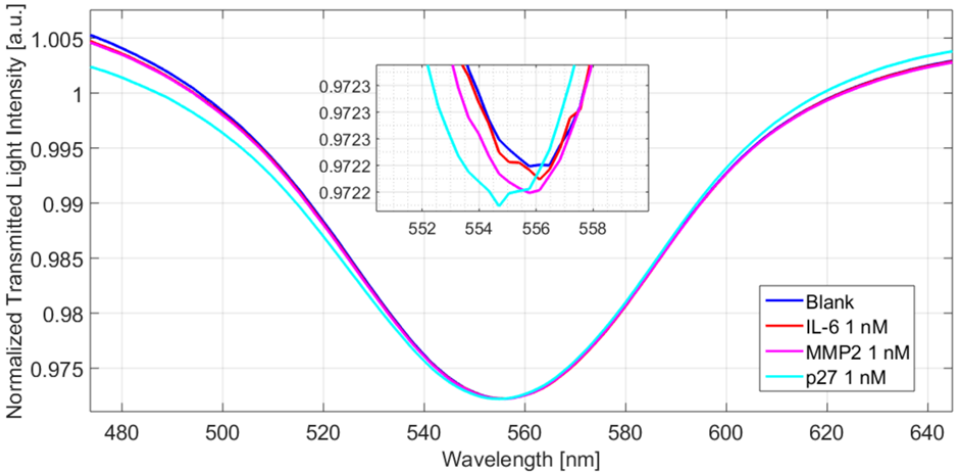

(a)

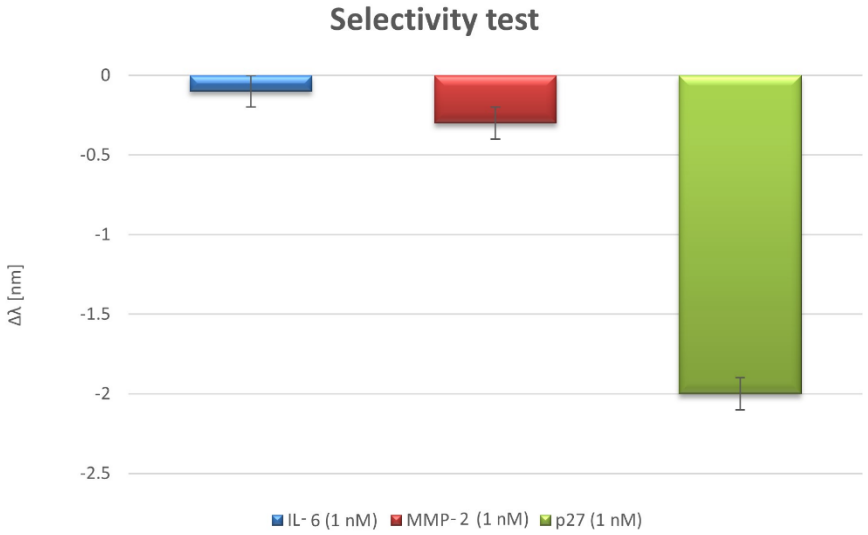

(b)

Fig. 12. (a) Normalized transmitted spectra obtained with the analyte (p27) and two interferents (MMP-2 and IL-6); (b) Experimental resonance wavelength variations (calculated with respect to the blank) for the three analyzed solutions.

process. In fact, in the case of the 3D-printed platform, a variation of the resonance wavelength of about 56 nm was obtained (see Fig. 10), while, typically, for the SPR-POF sensor, a shift was about 15 nm following the functionalization procedure [31,45]. On the other hand, the two results obtained are comparable in terms of LOD (tens of pM). In other words, the proposed 3D-printed biosensor presents a wide range of detection with respect to the reference SPR-POF biosensor.

For a comparison with the state of the art related to devices able to measure p27, no biosensors are described in the literature, to our knowledge. Therefore, we can only provide a comparison with commercially available ELISA (enzyme-linked immunoassay) kits. Considering the calculated parameters of the presented 3D-printed biosensor, we might conclude that they overlap with the ones obtained by ELISA used for quantifying human p27. More specifically, among

Biomedical Optics EXPRESS

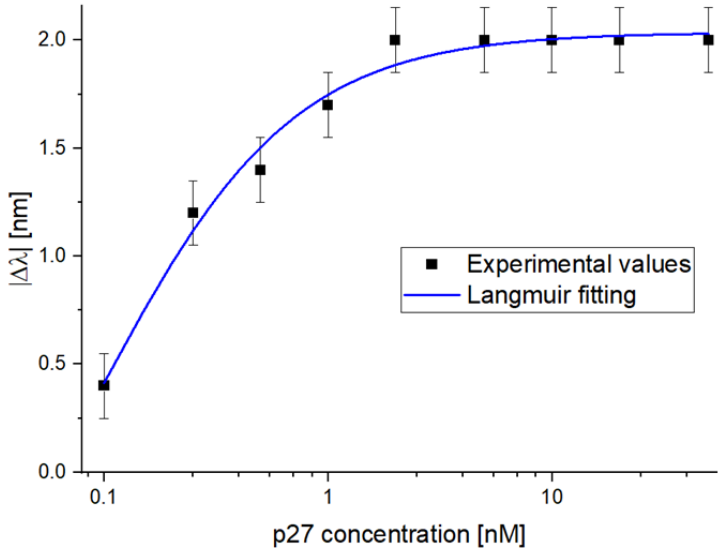

Fig. 13. Absolute value of the experimental variation in resonance wavelength (black marker), calculated with respect to the resonance wavelength of the blank, via a reference SPR-POF biosensor. The error bars and the Langmuir fitting (blue line) of the experimental values are also reported.

Table 4. Features related to SPR sensors based on optical adhesives, 3D-printed supports, and POF.

Sensor Configuration	Characteristics of the plasmonic probe	Remedial action	References
3D-printed platform based on an optimized core and gold film (the core refractive index is optimized to SPR)	• High sensitivity • Femtomolar range in the detection of substances • No metal bilayer is needed to improve the SPR performances • The optical adhesive presents a high shrinkage rate. • The metallic nanofilm adhesion is not excellent.	• The optical adhesive is jetted in two steps to obtain the desired waveguide's core thickness. • An intermediate buffer layer is necessary to improve the metal nanofilm adhesion.	[48,49]
3D-printed platform based on not-optimized core and metal bilayer	• The metallic nanofilm adhesion on the optical adhesive is good, thus no intermediate layer is necessary. • The optical adhesive presents a low shrinkage rate. • Good sensitivity • Picomolar range in the detection of substances	• The SPR performances have been improved by utilizing a metal bilayer.	This work

commercially available ELISA kits specific for human $p27^{Kip1}$, the detection ranges can vary from 15.63–1000 pg/mL (0.71-45.45 pM), with a sensitivity of 1–10 pg/mL, to ranges covering higher concentrations, such as 0.645–40 ng/mL (29.38 pM–1.81 nM), with a sensitivity of 0.1 to 1 ng/mL. Exploiting the proposed 3D-printed p27 biosensor, the obtained LOD is in a picomolar range with a wide linear range of detection if compared to the typical characteristics of the ELISA kits (used for instance by Moss S.C. et al. [46]) and to the reference SPR-POF biosensor.

Finally, it should be underlined that the combination of optical adhesives and 3D printing allows for tailoring the optical waveguide in terms of the light path for the equipment location

Biomedical Optics EXPRESS

and to improve the plasmonic performance. Along this line, Del Prete et al. recently presented an SPR sensor based on V-shaped waveguides achieved in 3D-printed support filled by a different optical adhesive [47]. For comparison, Table 4 summarizes the features of these two approaches to realize SPR sensors based on optical adhesives and 3D printing. As described in Table 4, the sensing configuration herein proposed denotes fewer fabrication issues (shrinkage and metal film adhesion) with respect to other configurations based on optical adhesives [48,49], even if the obtained sensitivity is lower than that achieved in [48,49], despite the fact that the metal bilayer increases the plasmonic performance. Nevertheless, as demonstrated in this work, the performances attained by this configuration are similar to those obtained by conventional SPR platforms (e.g., SPR D-shaped POF), with the advantage of avoiding polishing procedures (to obtain the D-shaped POF area) and spinning processes (to obtain the intermediate buffer layer).

6. Conclusion

Personalized medicine aims to treat diseases with tailored therapies and drugs according to each patient's needs. Advances in Next Generation Sequencing (NGS) technologies allow for the identification of gene mutations responsible for disease onset. Specifically, high throughput DNA sequencing can provide important diagnostic information by detecting genomic mutations, leading to an optimal drug selection for personalized cure [50,51]. DNA sequencing, however, is not appropriate for monitoring the effectiveness of the selected anticancer treatment. Instead, protein detection and quantitation are particularly advantageous since proteins directly mediate therapeutics' activities.

In this context, point-of-care (POC) technologies are increasingly significant for real-time biomarker measurements and self-monitoring therapy. From this point of view, we developed a novel metal bilayer-based plasmonic POC device exploiting additive manufacturing technology. The bulk sensitivity obtained by the proposed 3D-printed plasmonic probe via numerical and experimental results is comparable with other POF-based SPR sensors that require more complicated manufacturing processes. In the p27 detection, the tested 3D-printed SPR biosensor was shown a LOD value of 55 pM and a good selectivity. The obtained performance in terms of LOD was comparable to those achieved by commercially available ELISA kits, with the main advantages of a wide detection range and being portable and less expensive. Therefore, the proposed 3D-printed SPR biochip might be a disposable, low-cost sensor chip to assist therapeutic intervention.

Acknowledgments. The authors V.C. and N.C. acknowledge the CAMPANIA Project, VALERE program. E.S. acknowledges University of Campania Luigi Vanvitelli for "Kip2PTMCaTR" project (CUP: B63C22001470005). The authors L.Z. and L.A. acknowledge the EPI-MET Project founded by MIMIT. The authors N.C. and L.Z. acknowledge the support of the European Union by the Next Generation EU project PRIN2022 – 2022JRKETK – "BOHEMIAN" (Versatile hybrid in-fiBer Optical-electrocHemical systEMs for wIdely Applicable bioseNsing).

Disclosures. The authors declare that there are no conflicts of interest related to this article.

Data availability. Data underlying the results presented in this paper are not publicly available at this time but may be obtained from the authors upon reasonable request.

Supplemental document. See Supplement 1 for supporting content.

References

1. A. Lambert, S. Valiulis, and Q. Cheng, "Advances in Optical Sensing and Bioanalysis Enabled by 3D Printing," ACS Sens. **3**(12), 2475–2491 (2018).
2. Y. Xu, X. Wu, X. Guo, *et al.*, "The Boom in 3D-Printed Sensor Technology," Sensors **17**(5), 1166 (2017).
3. H.N. Chan, M.J.A. Tan, and H. Wu, "Point-of-Care Testing: Applications of 3D Printing," Lab Chip **17**(16), 2713–2739 (2017).
4. R.M. Dirkzwager, S. Liang, and J.A. Tanner, "Development of Aptamer-Based Point-of-Care Diagnostic Devices for Malaria Using Three-Dimensional Printing Rapid Prototyping," ACS Sens. **1**(4), 420–426 (2016).
5. D. Chudobova, K. Cihalova, S. Skalickova, *et al.*, "3D-printed Chip for Detection of Methicillin-resistant Staphylococcus Aureus Labeled with Gold Nanoparticles," Electrophoresis **36**(3), 457–466 (2015).

Biomedical Optics EXPRESS

6. N. Verma, S. Kumar, and H. Kaur, "Whole cell based disposable biosensor for Cadmium detection in milk," Adv. Appl. Sci. Res. **2**, 354–363 (2011).
7. M.M. Bordbar, A. Sheini, P. Hashemi, *et al.*, "Disposable paper-based biosensors for the point-of-care detection of hazardous contaminations—A review," Biosensors **11**(9), 316 (2021).
8. S. Malathi, I. Pakrudheen, S.N. Kalkura, *et al.*, "Disposable biosensors based on metal nanoparticles," Sens. Int. **3**, 100169 (2022).
9. B.C. Janegitz, J. Cancino, and V. Zucolotto, "Disposable biosensors for clinical diagnosis," J. Nanosci. Nanotechnol. **14**(1), 378–389 (2014).
10. J. Homola, "Surface plasmon resonance sensors for detection of chemical and biological species," Chem. Rev. **108**(2), 462–493 (2008).
11. F.S. Jahed and S. Hamidi, "Applications of surface plasmon resonance in human health care," Nanomedicine **15**(19), 1823–1827 (2020).
12. L Alwis, T. Sun, and K.T.V. Grattan, "Developments in optical fibre sensors for industrial applications," Opt. Laser Technol. **78**, 62–66 (2016).
13. Y Zhao, Z.Q. Deng, and Q. Wang, "Fiber optic SPR sensor for liquid concentration measurement," Sens. Actuators, B **192**, 229–233 (2014).
14. N. Cennamo, D. Massarotti, L. Conte, *et al.*, "Low-cost sensors based on SPR in a plastic optical fiber for biosensor implementation," Sensors **11**(12), 11752–11760 (2011).
15. J. Zhao, S. Cao, C. Liao, *et al.*, "Surface Plasmon Resonance Refractive Sensor Based on Silver-Coated Side-Polished Fiber," Sens. Actuators, B **230**, 206–211 (2016).
16. X.C. Yuan, B.H. Ong, Y.G. Tan, *et al.*, "Sensitivity–stability-optimized surface plasmon resonance sensing with double metal layers," J. Opt. A: Pure Appl. Opt. **8**(11), 959–963 (2006).
17. N. Cennamo, P. Zuppella, D. Bacco, *et al.*, "SPR sensor platform based on a novel metal bilayer applied on D–shaped plastic optical fibers for refractive index measurements in the range 1.38–1.42," IEEE Sens. J. **16**(12), 4822–4827 (2016).
18. J. Homola and M. Piliarik, *Surface Plasmon Resonance (SPR) Sensors* (Springer, 2006), pp. 45–67.
19. Y. Zhao, R.J. Tong, F. Xia, *et al.*, "Current status of optical fiber biosensor based on surface plasmon resonance," Biosens. Bioelectron. **142**, 111505 (2019).
20. A.K. Sharma, R. Jha, and B.D. Gupta, "Fiber-optic sensors based on surface plasmon resonance: a comprehensive review," IEEE Sens. J. **7**(8), 1118–1129 (2007).
21. Y. Zhao, Z. Q. Deng, and J. Li, "Photonic crystal fiber based surface plasmon resonance chemical sensors," Sens. Actuators, B **202**, 557–567 (2014).
22. A. K. Sharma, A. K. Pandey, and B. Kaur, "A review of advancements (2007–2017) in plasmonics-based optical fiber sensors," Opt. Fiber Technol. **43**, 20–34 (2018).
23. S. S. Hinman, K.S. McKeating, and Q. Cheng, "Plasmonic Sensing with 3D Printed Optics," Anal. Chem. **89**(23), 12626–12630 (2017).
24. N. Cennamo, L. Saitta, C. Tosto, *et al.*, "Microstructured Surface Plasmon Resonance Sensor Based on Inkjet 3D Printing Using Photocurable Resins with Tailored Refractive Index," Polymers **13**(15), 2518 (2021).
25. G. Cicala, F. Arcadio, L. Zeni, *et al.*, "Plasmonic Sensors based on 3D-printed polymer waveguides covered by a metals bilayer," IEEE Sensors Applications Symposium (SAS) **1**, 1–4 (2022).
26. D. Bencivenga, E. Stampone, D. Roberti, *et al.*, "p27Kip1, an Intrinsically Unstructured Protein with Scaffold Properties," Cells **10**(9), 2254 (2021).
27. D. Bencivenga, A. Tramontano, A. Borgia, *et al.*, "p27Kip1 serine 10 phosphorylation determines its metabolism and interaction with cyclin-dependent kinases," Cell Cycle **13**(23), 3768–3782 (2014).
28. V. Kumarasamy, P. Vail, R. Nambiar, *et al.*, "Functional Determinants of Cell Cycle Plasticity and Sensitivity to CDK4/6 Inhibition," Cancer Res. **81**(5), 1347–1360 (2021).
29. T. Higuchi, A. Takeuchi, S. Munesue, *et al.*, "A nonsteroidal anti-inflammatory drug, zaltoprofen, inhibits the growth of extraskeletal chondrosarcoma cells by inducing PPARγ," Cell Cycle **22**(8), 939–950 (2023).
30. S. Idris, B. Refaat, R.A. Almaimani, *et al.*, "Enhanced in vitro tumoricidal effects of 5-Fluorouracil, thymoquinone, and active vitamin D3 triple therapy against colon cancer cells by attenuating the PI3 K/AKT/mTOR pathway," Life Sci **296**, 120442 (2022).
31. N. Cennamo, A. Piccirillo, D. Bencivenga, *et al.*, "Towards a point-of-care test to cover atto-femto and pico-nano molar concentration ranges in interleukin 6 detection exploiting PMMA-based plasmonic biosensor chips," Talanta **256**, 124284 (2023).
32. M. M. Rahman, M. M. Rana, M. S. Rahman, *et al.*, "Sensitivity enhancement of SPR biosensors employing heterostructure of PtSe2 and 2D materials," Opt. Mater. **107**, 110123 (2020).
33. B. Meshginqalam and J. Barvestani, "Performance Enhancement of SPR Biosensor Based on Phosphorene and Transition Metal Dichalcogenides for Sensing DNA Hybridization," IEEE Sens. J. **18**(18), 7537–7543 (2018).
34. M. Kanso, S. Cuenot, and G. Louarn, "Sensitivity of Optical Fiber Sensor Based on Surface Plasmon Resonance: Modeling and Experiments," Plasmonics **3**(2-3), 49–57 (2008).
35. B. D. Gupta and A. K. Sharma, "Sensitivity Evaluation of a Multi-Layered Surface Plasmon Resonance-Based Fiber Optic Sensor: A Theoretical Study," Sens. Actuat. B Chem. **107**(1), 40–46 (2005).

Biomedical Optics EXPRESS

36. K. Balaa, M. Kanso, S. Cuenot, *et al.*, "Experimental Realization and Numerical Simulation of Wavelength-Modulated Fibre Optic Sensor Based on Surface Plasmon Resonance," Sens. Actuat. B Chem. **126**(1), 198–203 (2007).
37. R. Tabassum and B. D. Gupta, "SPR based fiber-optic sensor with enhanced electric field intensity and figure of merit using different single and bimetallic configurations," Opt. Commun. **367**, 23–34 (2016).
38. Q. Wang, X. Jiang, L.-Y. Niu, *et al.*, "Enhanced sensitivity of bimetallic optical fiber SPR sensor based on MoS_2 nanosheets," Opt. Lasers Eng. **128**, 105997 (2020).
39. Y. Chen, Y. Yu, X. Li, *et al.*, "Experimental Comparison of Fiber-Optic Surface Plasmon Resonance Sensors with Multi Metal Layers and Single Silver or Gold Layer," Plasmonics. **10**(6), 1801–1808 (2015).
40. Y. S. Dwivedi, A. K. Sharma, and B. D. Gupta, "Influence of Design Parameters on the Performance of a Surface Plasmon Sensor Based Fiber Optic Sensor," Plasmonics **3**(2-3), 79–86 (2008).
41. M. Iga, A. Seki, and K. Watanabe, "Gold thickness dependence of SPR-based hetero-core structured optical fiber sensor," Sens. Actuators B Chem. **106**(1), 363–368 (2005).
42. A. K. Sharma and B. D. Gupta, "On the sensitivity and signal to noise ratio of a step-index fiber optic surface plasmon resonance sensor with bimetallic layers," Opt. Commun. **245**(1-6), 159–169 (2005).
43. K. Gasior, T. Martynkien, and W. Urbanczyk, "Effect of constructional parameters on the performance of a surface plasmon resonance sensor based on a multimode polymer optical fiber," Appl. Opt. **53**(35), 8167 (2014).
44. S. M. Gan, P. S. Menon, N. R. Mohamad, *et al.*, "FDTD simulation of Kretschmann based Cr-Ag-ITO SPR for refractive index sensor," Mater. Today: Proc. **7**, 668–674 (2019).
45. D. Bencivenga, F. Arcadio, A. Piccirillo, *et al.*, "Plasmonic Optical Fiber Biosensor Development for Point-of-Care Detection of Malondialdehyde as a Biomarker of Oxidative Stress," Free Radic. Biol. Med. **199**, 177–188 (2023).
46. M. Thompson, S.L.R. Ellison, and R. Wood, "Harmonized Guidelines for Single-Laboratory Validation of Methods of Analysis (IUPAC Technical Report)," Pure Appl. Chem. **74**(5), 835–855 (2002).
47. S. C. Moss, D. J. Lightell Jr, S. O. Marx, *et al.*, "Rapamycin Regulates Endothelial Cell Migration through Regulation of the Cyclin-dependent Kinase Inhibitor p27Kip1," J. Biol. Chem. **285**(16), 11991–11997 (2010).
48. D. D. Prete, C. Marzano, F. Arcadio, *et al.*, "A Femtomolar Detection Range via Plasmonic Biosensors Based on V-Shaped Optical Adhesives Waveguides," IEEE Sens. J. **23**(24), 30325–30334 (2023).
49. F. Arcadio, C. Marzano, D. Del Prete, *et al.*, "Analysis of Plasmonic Sensors Performance Realized by Exploiting Different UV-Cured Optical Adhesives Combined with Plastic Optical Fibers," Sensors **23**(13), 6182 (2023).
50. C. Kim, R. Gao, E. Sei, *et al.*, "Chemoresistance Evolution in Triple-Negative Breast Cancer Delineated by Single-Cell Sequencing," Cell **173**(4), 879–893.e13 (2018).
51. M. I. Natalicchio, G. Improta, A. Zupa, *et al.*, "Pyrosequencing evaluation of low-frequency KRAS mutant alleles for EGF receptor therapy selection in metastatic colorectal carcinoma," Future Oncol. **10**(5), 713–723 (2014).